CFD–DEM SIMULATION OF AEOLIAN SAND TRANSPORT: EFFECTS OF WIND-SPEED AND SAND PARTICLE SHAPE
/
基于 CFD–DEM 的风沙输运模拟：风速与沙粒形状的影响

Fengrong LI, Afang JIN *), Bo YANG, Junhan LI, Junpeng YANG 1)
College of Mechanical Engineering, Xinjiang University, Urumqi 830046 / China;
Tel: +86-13999805154; E-mail: jinaf3500_xju@xju.edu.cn
DOI: https://doi.org/10.35633/inmateh-77-90

Keywords: *CFD-DEM, aeolian sand transport, superquadric particles, particle shape effects*

ABSTRACT

Aeolian sand transport is a key driver of desertification; however, accurately modeling particle–fluid interactions remains challenging. Many existing numerical simulations assume spherical grains, which can introduce systematic errors in transport predictions. To address this limitation, a CFD–DEM framework incorporating superquadric particles was developed, enabling a more realistic representation of grain geometry. Simulations were conducted at wind speeds of 9, 12, and 15 m/s, with systematic variations in particle axis ratio and shape parameters, and the results were validated against wind tunnel experiments. The results reveal a clear hierarchical control of aeolian transport dynamics. Wind speed dominates transport intensity and temporal evolution. The particle axis ratio exerts the primary influence on streamwise transport, producing variations of up to 96% in mean particle velocity, whereas shape parameters induce smaller changes of approximately 53%. In contrast, particle shape parameters govern vertical transport behavior, causing velocity variations of up to 91.6%, compared with less than 74.4% attributable to axis ratio effects. Moreover, the influence of shape parameters weakens with increasing wind speed, with maximum variations of 83%, 67%, and 59% at wind speeds of 9, 12, and 15 m/s, respectively. This study enhances the accuracy of wind-sand transport simulations and contributes to improved predictions of wind-driven sand impacts on soil, crops, and water resources in farmland. The improved simulations provide scientific support for agricultural wind and sand control and ecological restoration, promoting sustainable agricultural development and mitigating the negative effects of desertification.

摘要

风沙输运是荒漠化的主要驱动因素，但颗粒–流体相互作用的建模仍然具有挑战性。许多现有模拟假设沙粒为球形，这可能在输运预测中引入系统性误差。为克服这一局限，我们开发了一种结合超二次曲面颗粒的 CFD–DEM 框架，从而能够更真实地表征沙粒几何形态。模拟在 9、12 和 15 m/s 的风速下进行，系统考察了轴比和形状参数的变化，并通过风洞实验进行了验证。结果表明，输运动力学存在明显的分层控制效应。风速主导了输运强度和时间演化。轴比在顺风方向上起主要作用，平均速度变化幅度高达 96%；而形状参数的影响相对较小，约为 53%。相反，在垂直输运中，形状参数起决定性作用，速度变化幅度高达 91.6%，而轴比的影响小于 74.4%。随着风速增加，形状参数的影响逐渐减弱，在 9、12 和 15 m/s 下的最大变化分别为 83%、67% 和 59%。这项研究提高了风沙输送模拟的精度，帮助更好地预测风沙对农田土壤、作物和水资源的影响。改进的模拟为农业风沙控制和生态恢复提供了科学支持，推动可持续农业发展，并减轻沙漠化的负面影响。

INTRODUCTION

Land desertification is gradually evolving into one of the most destructive global ecological and social environmental issues of the 21st century *(AbdelRahman, 2023; Spinoni et al., 2021)*. Its continued expansion not only causes a sharp decline in land resources and degradation of ecosystem functions, but also significantly increases the probability of natural disasters *(Huang et al., 2016)*. Desertification poses a particularly serious threat to agricultural production because it directly affects the soil quality of farmland, the growing environment of crops, and the availability of water resources (*Dammala et al., 2025*). According to the latest assessment, by 2050, more than 75% of the global population will be directly or indirectly affected by desertification *(Akhtar-Schuster et al., 2022)*. Aeolian sand invasion is particularly severe in arid and semi-arid regions. The movement of aeolian sand accelerates the evolution of dune morphology and soil erosion through

Fengrong Li, M.S.stud; Afang Jin, Professor; Bo Yang, M.S.stud; Junhan Li, M.S.stud; Junpeng Yang,

gas-solid interactions, thereby threatening transportation, agricultural production, infrastructure construction, and regional socio-economic stability *(Zong & Wu, 2024)*.

Therefore, deeply studying the transport dynamics of aeolian two-phase flow not only has significant scientific value but also provides crucial theoretical support for desertification control, engineering protection, and regional sustainable development.

Since Bagnold established the foundation of wind-sand dynamics theory, the study of aeolian transport mechanisms has continuously developed. This development spans from experimental observations to theoretical modeling and numerical simulations *(Bagnold, 2012)*. Early studies primarily relied on wind tunnel experiments and field observations *(Anderson & Haff, 1988; Shao & Lu, 2000; Zhang et al., 2021)*. These studies systematically revealed the basic laws of wind-sand movement, including the critical initiation wind speed, saltation particle size distribution, and the relationship between wind speed and sand transport flux. With the development of computational fluid dynamics, researchers gradually introduced numerical methods to simulate wind-sand processes (*Song et al., 2018*). The gas-solid two-phase flow model and discrete element method (DEM) have become core tools in this research *(Yang et al., 2010)*. Related studies consistently show that the geometric properties of sand grains, such as particle size, aspect ratio, and surface roughness, significantly affect key dynamic processes (*Marshall et al., 2021*). These include the initiation threshold, saltation trajectory, and transport flux *(Liu et al., 2025)*. However, despite the widespread recognition of the importance of shape effects, most existing numerical models still simplify natural sand grains as ideal spheres (*Zheng & Hryciw, 2016*). This introduces systematic bias, which affects the accurate prediction of wind-sand transport in agricultural environments.

To overcome the limitations of the spherical assumption, scholars have proposed various non-spherical modeling methods *(Lv & Zhao, 2025)*. For example, Kruggel-Emden et al. used a combination of spheres to approximate irregular particles *(Kruggel-Emden et al., 2008)*. This method improved simulation accuracy to some extent, but it required many sub-spheres, leading to high computational costs. Wang et al. studied the critical conditions for wind-sand initiation based on the ellipsoid model *(Wang et al., 2014)*. They revealed that non-spherical particles have a higher initiation threshold than spherical particles. In recent years, Liu et al. proposed a multi-superellipsoid model to enhance the adaptability of DEM to complex shapes *(Liu & Zhao, 2020)*. Liu et al. attempted to combine polyhedral and ellipsoid models to improve geometric realism and reduce computational errors *(Liu et al., 2021)*. Although these studies have significantly advanced non-spherical particle modeling, they still face issues such as insufficient degrees of freedom in shape parameters, limited ability to represent complex geometries, and high computational costs.

Compared to other non-spherical modeling methods, the superquadric model exhibits greater flexibility in geometric description. This model requires only a few shape parameters to uniformly describe various typical geometries, such as spheres, ellipsoids, cubes, and prisms *(Qiao et al., 2022)*. It not only effectively improves the accuracy of sand grain shape representation but also captures complex surface features while maintaining high computational efficiency. Previous studies have shown that this model has good application prospects in fields such as powder mechanics and particle collisions *(Tang et al., 2024)*. However, existing research still lacks systematic exploration of incorporating the superquadric model into CFD–DEM wind-sand transport simulations. In particular, its regulatory mechanisms on sand grain dynamics under different wind speed conditions have not been quantitatively revealed.

Overall, existing numerical models still have shortcomings in describing the true geometric features of sand grains, which limits the in-depth understanding of wind-sand transport dynamics to some extent. To address this issue, this study introduces the superquadric function into the CFD-DEM coupled framework to construct a parameterized sand grain model. The aim is to investigate the effects of aspect ratio and shape factor on aeolian transport. By combining numerical simulation results under different wind speed conditions with wind tunnel experiments, the effectiveness of the model is verified. It further reveals how sand grain geometric parameters affect sediment transport flux, saltation velocity characteristics, and bed erosion processes. This research not only provides theoretical support for improving wind-sand simulation methods but also offers precise control strategies for agricultural wind-sand prevention and ecological restoration. It is especially helpful in reducing the negative impact of wind-sand on agricultural production.

MATERIALS AND METHODS

Sand grain modeling method

In numerical simulations of wind-sand transport, accurately describing the geometric features of sand grains is crucial for obtaining physically consistent computational results.

The shape of sand grains directly affects aerodynamic properties, saltation dynamics, and the interactions between particles and between particles and the fluid *(Zhang et al., 2025)*.

Traditional discrete element method (DEM) simulations usually simplify particles as spheres or combinations of spheres, but this idealization fails to reflect the non-spherical and irregular features of natural sand grains, thus introducing significant bias *(Podlozhnyuk et al., 2017)*. To overcome this limitation, this study introduces the superquadric modeling method. The implicit equation of the superquadric surface is:

$$\left(\left|\frac{x}{a}\right|^{n_2}+\left|\frac{y}{b}\right|^{n_2}\right)^{\frac{n_1}{n_2}}+\left|\frac{z}{c}\right|^{n_1}=1 \tag{1}$$

where: a is the semi-axis length along the x axis, [m]; b is the semi-axis length along the y axis, [m]; c is the semi-axis length along the z axis, [m]; n_1 is the shape factor controlling the curvature of the sand grains along the z axis, [dimensionless]; n_2 is the shape factor controlling the curvature of the sand grains along the x and y axes, [dimensionless].

By adjusting the above parameters, multiple sand grain models, ranging from nearly spherical to highly angular, can be generated, as shown in Fig. 1.

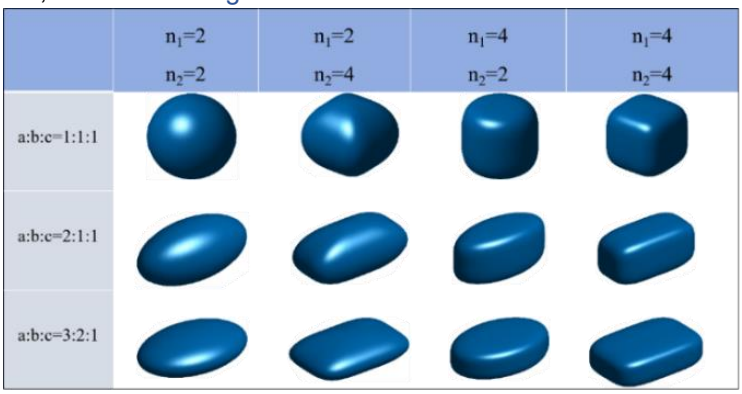

Fig. 1 - Geometric morphology of superquadric sand grains under different axis ratios and shape indices

To facilitate the DEM grid processing, the implicit equation can be transformed into an explicit parameter form:

$$\begin{aligned} X(\theta,\phi) &= a\cdot\mathrm{sgn}(\cos\theta)\cdot|\cos\theta|^{2/n_1}\cdot\mathrm{sgn}(\cos\phi)\cdot|\cos\phi|^{2/n_2} \\ Y(\theta,\phi) &= b\cdot\mathrm{sgn}(\cos\theta)\cdot|\cos\theta|^{2/n_1}\cdot\mathrm{sgn}(\sin\phi)\cdot|\sin\phi|^{2/n_2} \\ Z(\theta) &= c\cdot\mathrm{sgn}(\sin\theta)\cdot|\sin\theta|^{2/n_1} \end{aligned} \tag{2}$$

The expression $\theta\in[-\pi/2,\pi/2],\phi\in[0,2\pi]$ can directly generate high-resolution point clouds. After triangulation, an STL mesh file is constructed, which can seamlessly integrate with the CFD-DEM solver.

DEM particle dynamics equation

This paper uses the discrete element method (DEM) to explicitly solve the interactions between sand particles. In wind-sand saltation and rolling, the deformation of sand particles is negligible compared to their geometric size, so the sand particles are treated as ideal rigid bodies. This assumption not only reduces the computational cost but also ensures the accuracy of the dynamic predictions *(Zhu et al., 2007)*. The translational and rotational equations of the sand particles are as follows:

$$m\frac{dv}{dt}=F_c+F_g+F_d+F_b \tag{3}$$

$$I\frac{d\omega}{dt}=M_c+M_d \tag{4}$$

where: m is the mass of the sand particle, [kg]; v is the velocity of the sand particle, [m/s]; F_c is the contact force, [N]; F_g is the gravity, [N]; F_d is the drag force exerted by the fluid on the sand particle, [N]; F_b is the buoyancy, [N]; I is the moment of inertia tensor of the sand particle, [kg·m²]; ω is the angular velocity of the particle, [rad/s]; M_c is the contact torque, [N·m]; M_d is the contact torque, [N·m].

The collision contact mechanics use the Hertz-Mindlin (no-slip) contact model, which captures both normal and tangential elastic deformations and damping effects, and introduces the rolling friction torque *(Lu et al., 2015)*.

$$F_n = k_n \delta_n^{3/2} - \eta_n v_n \quad (5)$$

$$F_t = k_t \delta_t - \eta_t v_t \quad (6)$$

$$M_r = -\mu_r R F_n \quad (7)$$

where:

F_n is the normal contact force acting on the sand particle, [N]; F_t is the tangential contact force acting on the sand particle, [N]; M_r is the rolling resistance torque acting on the sand particle, [N·m]; δ_n is the normal overlap between the contacting particles, [m]; δ_t is the tangential overlap between the contacting particles, [m]; v_n is the normal relative velocity at the contact point, [m/s]; v_t is the tangential relative velocity at the contact point, [m/s]; k_n is the normal contact stiffness, [N/m$^{3/2}$]; k_t is the tangential contact stiffness, [N/m$^{3/2}$]; η_n is the normal damping coefficient, [N·s/m]; η_t is the tangential damping coefficient, [N·s/m]; μ_r is the rolling friction coefficient, [dimensionless]; R is the equivalent radius of the sand particle, [m].

CFD control equations

The gas-phase flow field is assumed to be an incompressible Newtonian fluid, and the Reynolds-averaged Navier–Stokes (RANS) equations are employed, coupled with the standard k–ε turbulence model for the solution *(Launder & Spalding, 1983)*. This combination effectively balances computational stability and efficiency when addressing turbulence structures dominated by near-surface shear. The continuity and momentum equations are as follows:

$$\frac{\partial \rho}{\partial t} + \nabla \cdot (\rho u) = 0 \quad (8)$$

$$\frac{\partial (\rho u)}{\partial t} + \nabla \cdot (\rho u u) = -\nabla p + \nabla \cdot \tau + S_m \quad (9)$$

where: ρ is the fluid density, [kg/m^3]; u is the fluid velocity, [m/s]; p is the pressure, [Pa]; τ is the stress tensor, [Pa]; and S_m is the momentum source term due to the particles, used to represent the inertial force, [N/m^3].

In turbulence modeling, based on the assumption that turbulence is locally homogeneous and isotropic, this study uses the standard turbulence model to solve the viscosity coefficient of the gas-phase turbulence (*Cao et al., 2022*). The equations of turbulent kinetic energy and turbulence dissipation rate are as follows:

$$\frac{\partial (\rho k)}{\partial t} + \nabla \cdot (\rho u k) = P_k - \rho \varepsilon + \nabla \cdot \left(\left(\mu + \frac{\mu_t}{\sigma_k} \right) \nabla k \right) \quad (10)$$

$$\frac{\partial (\rho \varepsilon)}{\partial t} + \nabla \cdot (\rho u \varepsilon) = C_1 \frac{\varepsilon}{k} P_k - C_2 \rho \frac{\varepsilon^2}{k} + \nabla \cdot \left(\left(\mu + \frac{\mu_t}{\sigma_\varepsilon} \right) \nabla \varepsilon \right) \quad (11)$$

where: k is the turbulent kinetic energy, [m^2/s^2]; ε is the turbulence dissipation rate, [m^2/s^3]; P_k is the turbulent kinetic energy generation term, [m^2/s^3]; μ_t is the fluid turbulent viscosity coefficient, [Pa·s]; σ_k is the turbulence Prandtl number for k, [dimensionless]; σ_ε is the turbulence Prandtl number for ε, [dimensionless]; C_1 is an empirical constant, [dimensionless]; C_2 is an empirical constant, [dimensionless].

Boundary condition setup

To accurately reproduce the wind tunnel experimental conditions and capture the subtle gas-particle interactions near the ground in the wind-sand flow, a three-dimensional CFD-DEM coupled computational domain was established. The computational domain measures 5×0.6×0.6 m (length × width × height), which includes a 1.0-meter development section and a 4.0-meter transport section in Fig. 2(a). A flat sand bed of 0.1 m × 0.1 m was placed between x = 1.0 m and x = 1.1 m, serving as the starting region for transport. The mesh used structured hexahedral elements, with refinement near the bed layer ($z \leq 0.15$ m) to accurately resolve the strong shear flow near the ground and the particle initiation process. The minimum cell size was 4 mm, gradually increasing to 8 mm, with a total of approximately 1.18×107 cells. To verify grid independence (under a wind speed of 9 m/s), a grid independence analysis was conducted in Fig. 2(b), with the average velocity of the sand particles at the outlet selected as the main comparison index. The analysis results show that when the number of cells exceeds 1.18×10^7, the change in sand particle velocity is less than 2.7%, indicating that this grid division scheme achieves a reasonable balance between computational accuracy and efficiency.

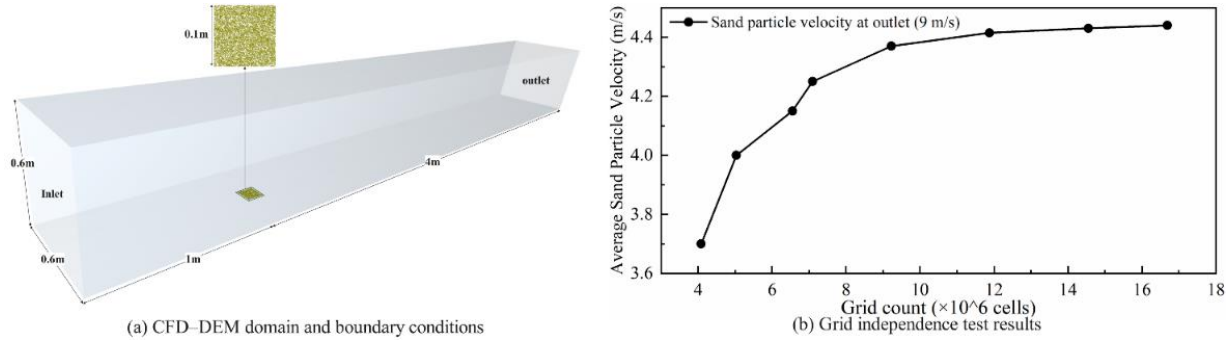

(a) CFD–DEM domain and boundary conditions (b) Grid independence test results

Fig. 2 - Boundary Condition Setup and Grid Independence Verification

Setting parameters

Table 1 lists the main physical models and parameters used in the CFD-DEM simulation. In the CFD part, the fluid was treated as an incompressible Newtonian fluid. The standard k–ε turbulence model was used. An enhanced wall treatment was applied to solve the Reynolds-averaged Navier–Stokes (RANS) equations. This method has been widely used for near-wall turbulence simulation. The inlet velocities were set to 9, 12, and 15 m/s. The turbulence intensity was set to 5%. The turbulent viscosity ratio was set to 10%. These conditions are commonly used in CFD-DEM studies of particle–fluid flow. The CFD time step was set to 100 times the DEM time step.

This setting ensures both numerical stability and computational efficiency. Such a treatment is common in previous CFD-DEM coupling studies. To calibrate the contact parameters in the DEM model, a funnel deposition method was used to conduct a repose angle test. As shown in Fig. 3, sand particles fall from a funnel and accumulate on a flat plate to form a conical sand pile. The static repose angle was obtained by measuring the slope of the sand pile surface. The experimental result was about 32°. Based on this result, the static friction coefficient and rolling friction coefficient were adjusted step by step. This ensured that the simulation reproduced the repose angle observed in the experiment. The calibrated contact parameters are shown in Table 1. These parameters ensure the physical reliability of the DEM simulation results.

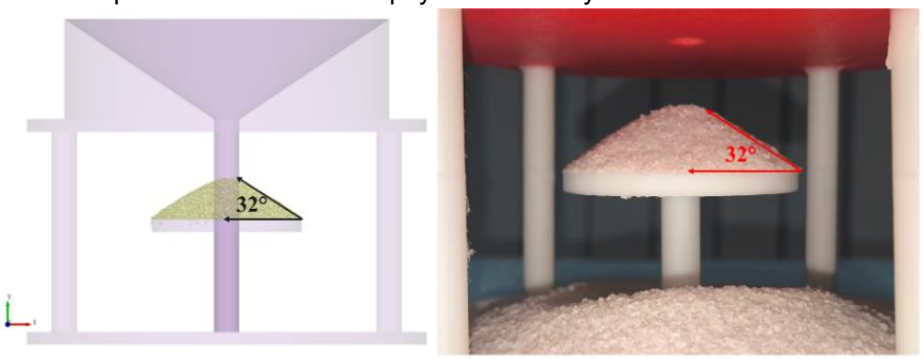

(a)Simulated repose angle of particles (b)Measured repose angle from experiment

Fig. 3 - Calibration of angle of repose parameters

Table 1

Key parameters of the DEM model

CFD parameter	Value	DEM parameters	Value
Method	CFD-DEM	Equivalent sphere radius[um]	300
Fluid velocity [m/s]	9,12,15	Poisson's ratio of sand grains	0.3
Air density [kg/m^3]	1.225	Solids density of sand grains [kg/m^3]	2600
Fluid viscosity [kg/m s]	1.789×10^{-5}	Shear modulus of sand grains [Pa]	4×10^{10}
Turbulence model	Standard k- ε model	Coefficient of restitution (P–P)	0.6
Inlet turbulent intensity [%]	5	Coefficient of static friction (P–P)	0.5
Inlet turbulent viscosity ratio	10	Coefficient of rolling friction (P–P)	0.07
Outlet turbulent intensity [%]	5	Poisson's ratio of steel	0.3
Outlet turbulent viscosity ratio	10	Solids density of steel [kg/m3]	7865
Drag model	Ganser drag	Shear modulus of steel [Pa]	7.9×10^{10}
Lift model	Saffman and magnus lift	Coefficient of restitution (P–W)	0.6
Fluid flow time step [s]	1×10^{-5}	Coefficient of static friction (P–W)	0.5
DEM time step [s]	1×10^{-7}	Coefficient of rolling friction (P–W)	0.05

Wind tunnel experiment setup

The experiments were conducted in a laboratory-built direct-current wind tunnel with a four-meter test section and a 0.6 × 0.6 m² cross-section. Transparent sidewalls provided undistorted optical access for PIV measurements, and the incoming flow was controlled through a closed-loop system that maintained stable operating conditions. Pressure and thermal anemometry were used to calibrate the flow before data collection. The general layout of the experimental setup is shown in Fig. 4, and the instruments used in the system are summarized in Table 2.

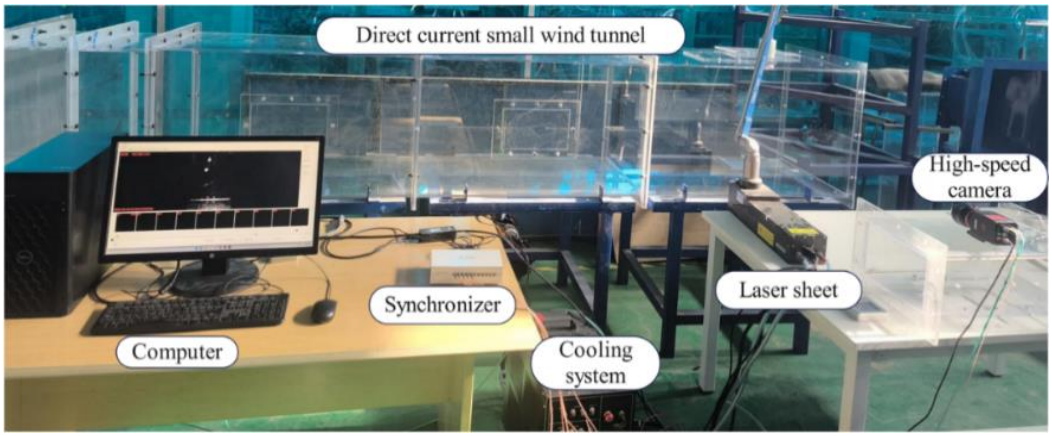

Fig. 4 - Wind tunnel experiment

A dual-pulse laser was employed to produce the light sheet illuminating the particles in the measurement plane. Its alignment and thickness were adjusted until a uniform sheet intersected the center of the test section. A high-speed camera viewed the illuminated region through the sidewall, and its exposure timing was synchronized with the laser pulses via an external controller to ensure accurate separation between the two frames. Quartz sand particles, sieved to a diameter range of 0.55–0.65 mm, served as the seeding material. Their size provided good image visibility and a rapid response to the airflow, and the particles were introduced upstream to promote homogeneous mixing before reaching the light sheet.

Table 2

Instrumentation used in the wind tunnel and PIV measurement system

Equipment	Model	Manufacturer / Country	Uncertainty
Direct-current small wind tunnel	4m×0.6m×0.6m	Laboratory-built	
Variable-frequency drive (VFD)	EN600-4T0055G/0075P	Eenergy (China)	±0.5%
Pitot-static tube	PTL-08 Series	Yiyong Instrument (China)	±1.0% (typical)
Hot-wire anemometer	TSI 1050	TSI (USA)	±1.5% (typical)
SDouble-pulse Nd:YAG laser	532 nm	Zhongke Feixiang (China)	±2% (energy stability)
Laser fiber	SMA905 / F8 NC/4A	Zhongke Feixiang (China)	
Sheet-forming optics	SF-100	Zhongke Feixiang (China)	
High-speed camera	VShot-200	Zhongke Feixiang (China)	±0.5 μs (timing)
Camera lens	SM series	Zhongke Feixiang (China)	
Camera mount	C-mount	Zhongke Feixiang (China)	
Synchronizer	Precision T3660	Zhongke Feixiang (China)	
Data workstation	Precision Tower T3660	Dell (USA)	
Photoelectric trigger	PE-200	Zhongke Feixiang (China)	
Quartz sand	38–46 mesh		
PIV processing software	PIV2D2C-FR	Zhongke Feixiang (China)	±3.7% (velocity)

Image sequences were recorded once steady flow was achieved. Background subtraction was applied prior to velocity extraction, and a hybrid PIV–PTV method was used to resolve the velocity field across regions of varying particle density. Spurious vectors were removed using median filtering, after which the valid vectors were mapped onto a uniform grid and averaged in time to obtain the final velocity distribution. The combined measurement uncertainty of the velocity field was about 3.7%, reflecting contributions from particle positioning, pulse timing, and vector matching. Additional uncertainties associated with the instruments and optical components are listed in Table 2.

RESULTS AND ANALYSIS

Model validation

Fig. 5 shows the instantaneous velocity distribution of sand particles at 10 vertical profile measurement points from the initial sand bed position to the wind tunnel outlet under wind speeds of 9, 12, and 15 m/s, compared with the wind tunnel experimental results. Overall, the numerical simulation and experimental measurements show consistent trends in the instantaneous velocity changes of sand particles, indicating that the model can effectively capture the response characteristics of the wind on the transport dynamics of particles with different shapes. Further analysis reveals that the numerical simulation results are generally slightly higher than the experimental measurements, with a maximum error of 24.7% at the wind tunnel outlet under a wind speed of 15 m/s. At lower wind speeds (9 m/s) and near the sand bed, the error is generally less than 10%. The main causes of the error may include the following: first, under high wind speed conditions, PIV measurements are affected by the turbulence intensity of the flow field and the uncertainty in tracer particle identification, which may lead to positioning errors. Secondly, the standard turbulence model has limitations in depicting turbulence anisotropy and energy dissipation in high shear regions, which affects simulation accuracy. Finally, although superellipsoidal shapes better reflect the dynamic behavior of sand particles compared to spherical shapes, the existing drag models still have some deviations in predicting particle drag under high Reynolds number conditions. Overall, the consistency between the numerical model and wind tunnel experimental data indicates that the proposed model can simulate the wind-sand transport process well, despite some errors, which are within a reasonable range. In the future, the simulation accuracy can be further improved by refining the turbulence and drag models.

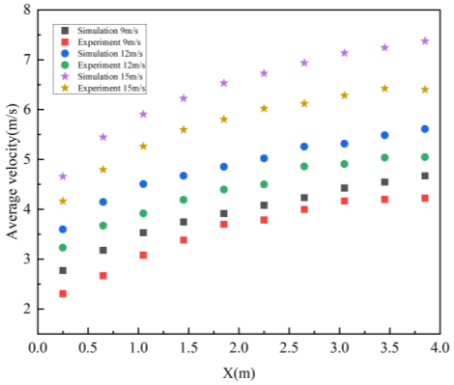

Fig. 5 - Comparison of experimental and simulated mean sand particle velocities

Effects of wind speed and particle shape on sand transport

Fig. 6 shows the temporal evolution characteristics of sand transport flux per unit time at the outlet section under three wind speed conditions. As the wind speed increases, the peak output flux increases significantly, and the overall process exhibits a typical three-stage evolution pattern: acceleration, stability, and decay. At a wind speed of 9 m/s, the sand transport flux increases slowly and quickly reaches a stable state, indicating that the system is near the critical transport threshold. The output flux does not reach higher levels, reflecting that the wind speed is insufficient to sustain continuous particle saltation. When the wind speed increases to 12 m/s, the flux growth rate accelerates significantly, with both the peak and steady-state levels being significantly higher than under lower wind speed conditions.

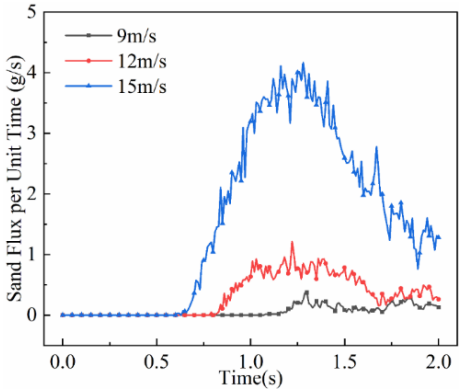

Fig. 6 - Temporal evolution characteristics of sand transport flux at different wind speeds

This indicates that the wind speed is sufficient to sustain continuous particle saltation and stable transport. As the wind speed further increases to 15 m/s, the output flux curve shows a sharp rise, reaching a high peak, followed by a non-steady-state decay phase. This change reflects the significant increase in particle saltation frequency, the rapid expansion of the transport scale, and the system's self-adjustment process under strong wind. At the same time, the collision effect between turbulence and particles provides additional energy input, facilitating the accelerated transport of sand particles. The numerical simulation results accurately reproduce the reinforcing effects of increased wind speed on the output flux and the wind-sand system's erosion, transport, and deposition processes.

Fig. 7(a) shows the cumulative mass distribution of sand particles with different shapes at the outlet over the 0–2 s time window under wind speeds of 9, 12, and 15 m/s. As the wind speed increases, the cumulative mass rises monotonically, indicating that stronger incoming flow energy increases the probability of sand particles overcoming the initiation threshold and maintaining transport. To remove the magnitude differences caused by wind speed, the cumulative mass is normalized before further analysis.

Fig. 7(b) normalizes the cumulative mass within the same time window based on each wind speed reference value, highlighting the role of the axis ratio (a:b:c). When the axis ratio increases from 1:1:1 to 3:2:1, the normalized cumulative mass decreases overall. The decrease is most pronounced at 9 m/s, which is consistent with the feature that near-bed shear stress is close to the sand particle initiation threshold under low wind speed and is more sensitive to shape parameters. The mechanism is that axial elongation enhances geometric anisotropy and bed interlocking contact, increasing rolling and overturning resistance and enhancing collision dissipation. At the same time, changes in projected area and lever arm increase the aerodynamic force required for initiation and sustained saltation, thereby reducing the effective flux.

Fig. 7(c) shows the normalized results for different Shape Parameters ($n1$, $n2$). The overall variation is smaller than the difference caused by the axis ratio, indicating that the Shape Parameters mainly have a secondary effect. Only when the axis ratio is low (1:1:1), changes in curvature and angularity have a more significant impact on cumulative mass, reflecting fine-scale correction of the transport process by adjusting the local drag coefficient and contact restitution characteristics. In summary, the outlet cumulative flux within the 0–2 s time window is mainly controlled by the combined effects of wind speed and axis ratios. The Shape Parameters play a supplementary fine-tuning role and are insufficient to alter the overall trend.

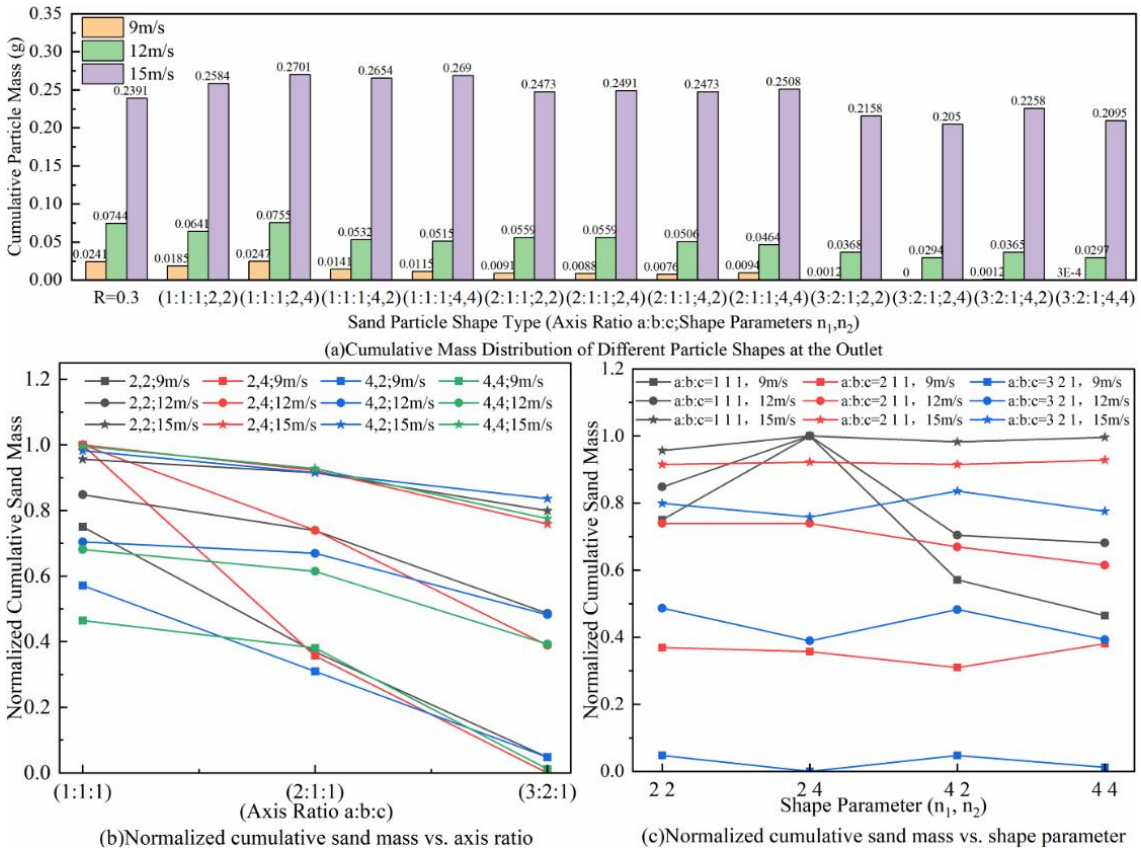

Fig. 7 - Effect of sand particle shape on cumulative mass distribution under different wind speeds

Mechanism of horizontal velocity under the coupled influence of wind speed and sand particle shape

Fig. 8 shows the variation of the average wind speed of sand particles with different shapes along the main horizontal direction over time under different wind speed conditions (9, 12, and 15 m/s). As the wind speed increases, the sand particle average velocity growth rate and peak increase significantly, indicating that wind speed has a decisive influence on sand particle motion. In all subplots, the average wind speed generally shows an increasing-decreasing trend, indicating that wind speed not only drives the acceleration of sand particles but also, at high wind speeds, causes the particles to gradually reach stability or decelerate through different dynamic mechanisms. The average velocity differences of sand particles with different axis ratios (a:b:c) are significant at each time point, especially under lower wind speed conditions, where the differences are more pronounced. Further analysis shows that as the axis ratio increases, the growth rate and peak of the sand particle average velocity gradually decrease.

This phenomenon can be attributed to changes in sand particle shape. As the axis ratio increases, the geometric symmetry of sand particles weakens, leading to enhanced anisotropy. The interaction between particles changes from point contact to surface contact, thereby increasing the self-locking effect, improving pile stability, and raising the initiation threshold. In addition, each subplot in Fig. 10 also shows the sand particle motion characteristics under different shape parameters ($n1$,$n2$). The results show that changes in shape parameters cause differences in the average velocity amplitude of sand particles with different axis ratios, indicating that shape parameters and axis ratios work together to significantly adjust the motion characteristics of sand particles. Although shape parameters have some effect on sand particle motion, their impact is more limited compared to the axis ratio. Their effect is mainly reflected in the micro-adjustment of sand particle motion, without altering the dominant influence of wind speed and axis ratios on the transport process.

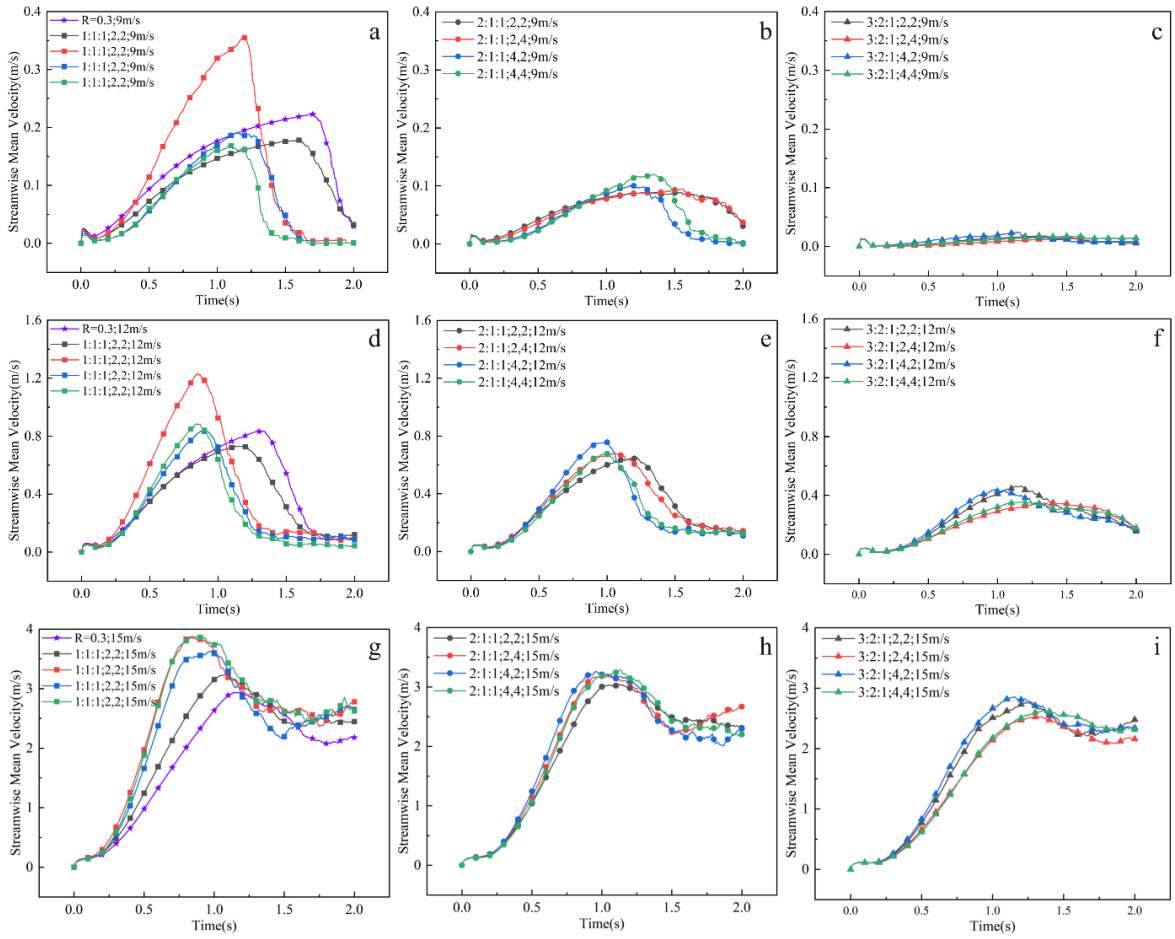

Fig. 8 - Temporal evolution of average wind speed along the main horizontal direction under different wind speeds and shapes of sand particles

Fig. 9(a) shows the trend of normalized peak average velocity along the main flow direction for superellipsoidal sand particles as the axis ratio (a:b:c) changes under wind speeds of 9, 12, and 15 m/s. To eliminate the influence of wind speed, the normalized peak velocity is calculated as a ratio based on the

maximum velocity at the same wind speed. The normalization results show that as the axis ratio increases from 1:1:1 to 3:2:1, the normalized peak velocity decreases significantly, especially at low wind speeds (9 m/s), where the peak change is most significant when the shape parameters are (2,4). Specifically, when axis ratios are 1:1:1, 2:1:1, and 3:1:1, the normalized peaks are 1, 0.26, and 0.04, with variation ranges of 74% and 96%, and absolute differences of 0.74 and 0.96, respectively. In contrast, sand particles with shape parameters (2,2) show smaller variations under high wind speeds (15 m/s).

Under different axis ratio conditions, the peaks are 0.83, 0.78, and 0.71, with variation ranges of 6% to 14%, and absolute differences of 0.05 to 0.12. This indicates that as the axis ratio increases, the sand particle shape changes from symmetric to asymmetric, leading to an increase in packing density, enhanced contact area and friction between particles, and a higher initiation threshold. Low-axis-ratios sand particles are more sensitive to changes in wind speed, while high-axis-ratios sand particles exhibit stronger structural locking effects, leading to delayed migration responses. Fig. 9(b) further explores the effect of shape parameters on the normalized peak average velocity along the main flow direction for sand particles with different axis ratios. Overall, an increase in shape parameters leads to a gradual rise in the peak of most sand particle shapes. Specifically, for sand particles with an axis ratio of 1:1:1, the peak variation ranges are 53%, 41%, and 17% under wind speeds of 9, 12, and 15 m/s, with absolute differences of 0.53, 0.41, and 0.17, respectively. For sand particles with an axis ratio of 2:1:1, the peak variation ranges are 25%, 14%, and 7%, with absolute differences of 0.08, 0.09, and 0.06, respectively. For sand particles with an axis ratio of 3:2:1, the peak variation ranges are 38%, 25%, and 11%, with absolute differences of 0.02, 0.09, and 0.08. The results show that shape parameters have a significant effect on the average velocity of sand particles with low axis ratios, while their effect on sand particles with high axis ratios is smaller. In addition, as the wind speed increases, the effect of shape parameters on sand particle average velocity gradually weakens.

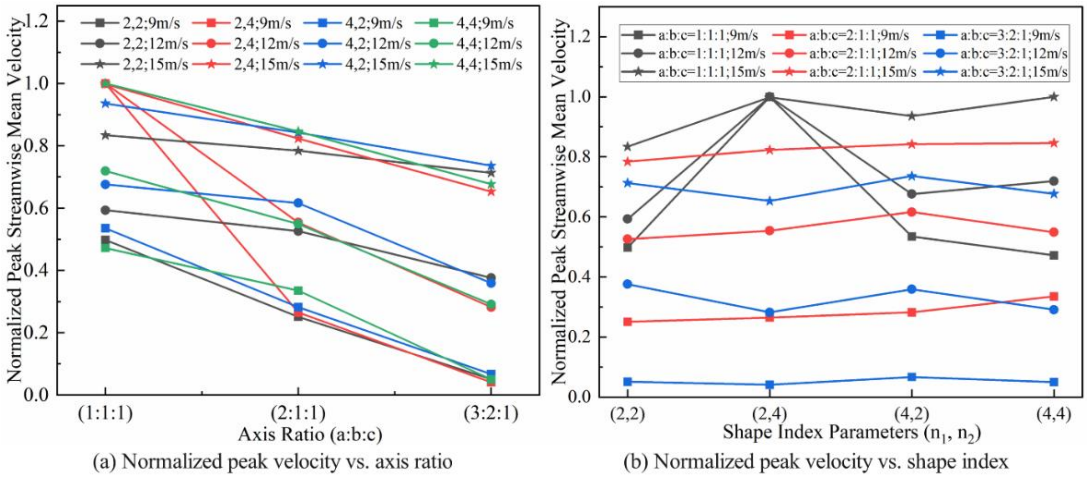

Fig. 9 - Variation of Normalized Peak Velocity of Different Sand Particle Shapes along the Main Flow

Fig. 10 shows the evolution of the maximum velocity along the streamwise direction for sand particles with different shapes under different wind speed conditions. Analysis shows that for sand particles with an axis ratio of 1:1:1, the peak velocity of sand particles with shape parameters (2,2) is significantly lower than that of other shape parameters, while the peak velocity differences between the other shape parameters are small, with a maximum variation of only 1.45%.

Under wind speeds of 9, 12, and 15 m/s, the maximum peak velocity variation of sand particles with shape parameters (2,2) is 39.8%, 18.1%, and 6.7%, respectively, compared to other shape parameters. Sand particles with shape parameters (2,2) exhibit lower peak velocities, mainly because their geometric shape is more symmetric and their surface curvature is gentler. The lower surface curvature leads to a smaller contact area between the airflow and sand particles, thereby weakening the interaction between the particles and the airflow, and reducing friction and drag. Therefore, under the influence of wind speed, these sand particles struggle to gain sufficient acceleration, resulting in lower peak velocities. In contrast, sand particles with other shape parameters typically have higher surface curvature, increasing the contact area with the airflow, strengthening friction and drag, and ultimately promoting sand particle acceleration, leading to significantly higher peak velocities.

For particles with an axis ratio of 2:1:1, the peak velocity increases with shape parameters, reaches the maximum at shape parameters (4,2), and then begins to decrease.

At wind speeds of 9, 12, and 15 m/s, the maximum peak velocity variation is 17.9%, 16.0%, and 6.5%, respectively. For particles with an axis ratio of 3:2:1, the peak velocities for shape parameters (4,2), (2,2), (4,4), and (2,4) show a decreasing trend, with maximum variations of 74.8%, 2.7%, and 5.3%, respectively. Overall, the results indicate that as the axis ratio and wind speed decrease, the influence of shape parameters on the maximum streamwise velocity of sand particles gradually weakens.

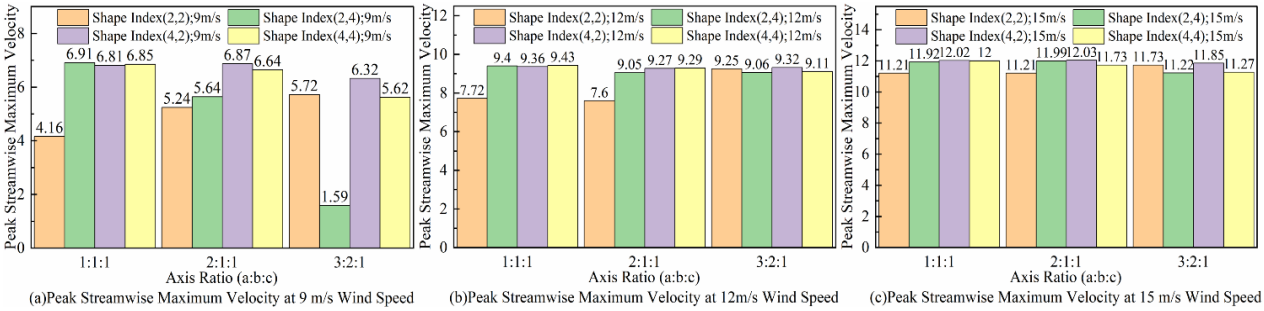

Fig. 10 - Streamwise peak velocity under different wind speeds and sand particle shapes

Mechanism of vertical velocity variation under the coupled effect of wind speed and sand particle shape

Qualitative analysis of Fig. 11 shows that as wind speed (9, 12, 15 m/s) increases, the vertical average velocity of sand particles rises significantly, and the time to reach the saltation peak occurs earlier, highlighting the dominant role of wind speed in driving the saltation process of sand particles. Higher wind speeds not only accelerate the saltation velocity of sand particles but also shorten the response time, thereby enhancing vertical migration ability. Under the same wind speed conditions, the vertical velocity decreases as the axis ratio increases. This trend is caused by the bed arching effect and self-locking effect induced by the increase in axis ratios, which makes high-axis-ratio sand particles need to overcome a higher critical wind speed to initiate saltation. For low-axis-ratio (1:1:1) particles, an increase in shape parameters leads to a decrease in sphericity and an increase in drag, which enhances vertical velocity and promotes saltation. High-axis-ratio particles experience significant resistance due to the packing structure, requiring higher wind speeds to initiate saltation. Overall, wind speed and sand particle shape parameters (axis ratio and shape parameters) have a significant impact on saltation behavior and vertical migration ability. An increase in wind speed significantly accelerates saltation response, while shape characteristics regulate sand particle saltation efficiency and dynamic performance to some extent.

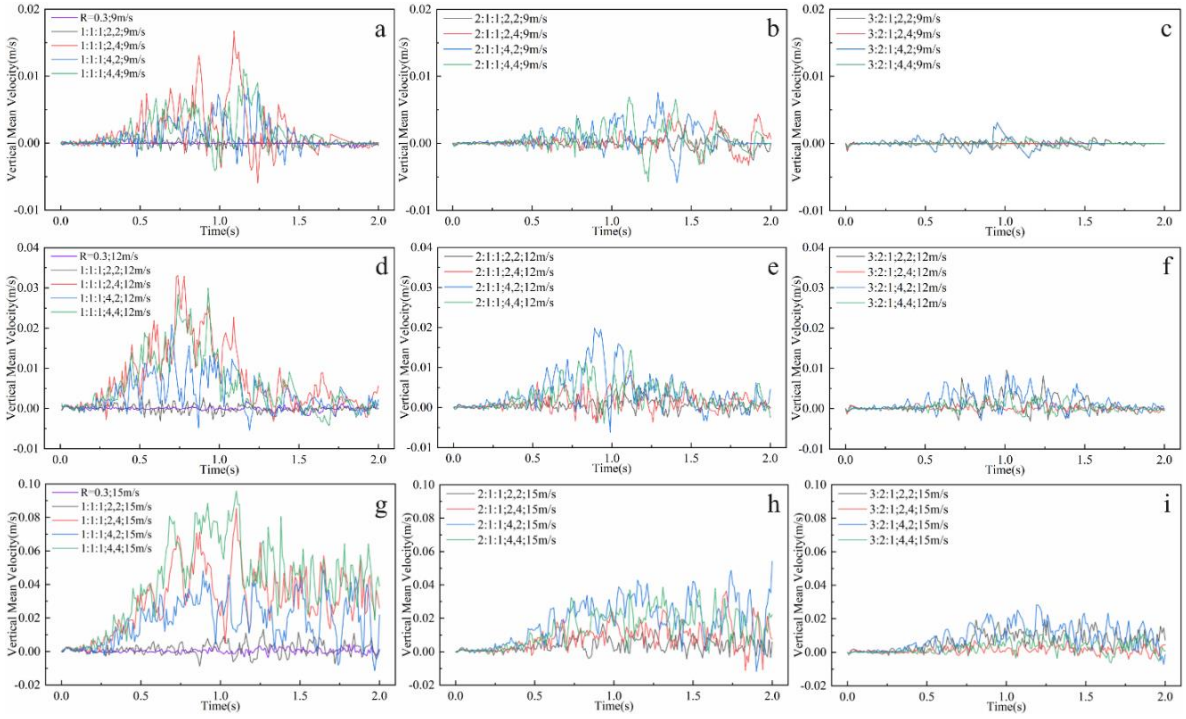

Fig. 11 - Vertical average velocity response of sand particles with different shapes under different wind speed conditions

Fig. 12(a) presents the variation characteristics of the normalized vertical average velocity peak for sand particles with different shape parameters under various axis ratio conditions. The results show that sand particles with shape parameters (2,2) exhibit a continuous increase as the axis ratio increases, with this effect being particularly significant under high wind speed conditions.

For example, when the wind speed is 15 m/s and the axis ratio increases from 2:1:1 to 3:2:1, the normalized peak velocity increases by 15%, with an absolute difference of 0.031. In contrast, sand particles with other shape parameters generally show a decrease in peak velocity as the axis ratio increases, with the variation being most significant for shape parameters (2,4). At a wind speed of 12 m/s, when the axis ratio increases from 1:1:1 to 2:1:1, the peak velocity decreases by 74.4%, with an absolute difference of 0.744. On this basis, Fig. 12(b) further investigates the modulation pattern of the shape parameters on the normalized vertical velocity peak. The results show that under the same axis ratio conditions, the peak velocity first increases and then decreases as the shape parameters increase. Quantitative analysis shows that when the axis ratio is 1:1:1 and the wind speed is 9 m/s, the largest increase in peak velocity occurs when the shape parameters change from (2,2) to (2,4), with an increase of 91.6% (absolute difference of 0.916). The largest decrease occurs when the shape parameters change from (2,4) to (4,2), with a decrease of 50.9% (absolute difference of 0.509). When the axis ratio is 2:1:1 and the wind speed is 12 m/s, the largest increase in peak velocity occurs when the shape parameters change from (2,4) to (4,2), with an increase of 59% (absolute difference of 0.354). The largest decrease occurs when the shape parameters change from (4,2) to (4,4), with a decrease of 27.7% (absolute difference of 0.166). When the axis ratio is 3:2:1 and the wind speed is 9 m/s, the largest increase in peak velocity occurs when the shape parameters change from (2,4) to (4,2), with an increase of 96.2% (absolute difference of 0.179). The largest decrease occurs when the shape parameters change from (2,2) to (2,4), with a decrease of 88.3% (absolute difference of 0.053). From the above results, it can be concluded that although changes in axis ratio affect the vertical peak velocity of sand particles to some extent, the overall impact is significantly weaker than the effect of shape parameters. Especially under the same wind speed conditions, the velocity variation caused by the shape parameters is significantly greater than the axis ratio effect, indicating that particle geometry plays a more significant role in the vertical momentum transfer process.

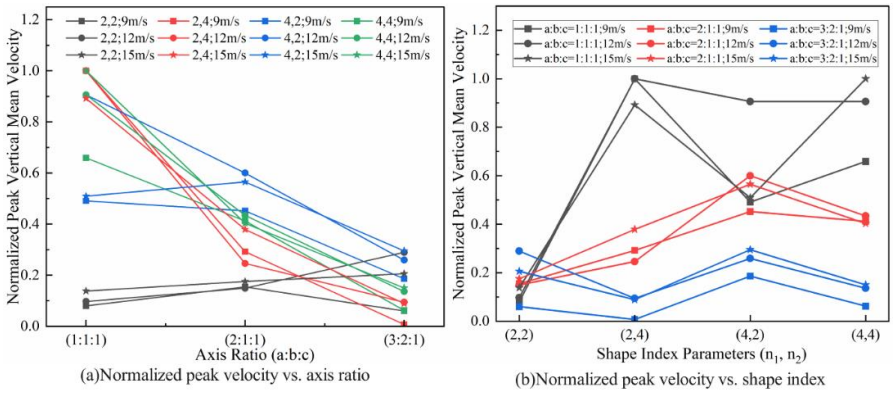

Fig. 12 - Variation of normalized peak velocity in the vertical direction for sand particles with different shapes

Fig. 13 shows the variation of vertical maximum velocity for sand particles with different shapes under wind speeds of 9, 12, and 15 m/s. Overall, an increase in wind speed significantly enhances the vertical maximum velocity of sand particles, highlighting the dominant role of wind speed in vertical motion. As the wind speed increases, the aerodynamic effect, especially the vertical thrust, is enhanced, significantly improving the vertical acceleration capacity of sand particles. The analysis shows that for sand particles with shape parameters (2,4), (4,2), and (4,4), the vertical maximum velocity decreases as the axis ratio increases. This is because an increase in axis ratio makes the sand particle shape more asymmetric or flattened, altering the airflow structure, weakening lift, and increasing lateral disturbance forces, ultimately reducing vertical thrust. In contrast, for sand particles with shape parameters (2,2), the vertical maximum velocity increases as the axis ratio increases.

At this point, the geometric shape of the sand particles becomes more symmetric and elongated in the longitudinal direction, increasing the surface area and thus improving the momentum exchange efficiency with the airflow. Under the same axis ratio, the vertical maximum velocity shows an overall increasing trend with the increase in shape parameters, but this effect gradually weakens as wind speed increases. Under wind speeds of 9, 12, and 15 m/s, the maximum variation caused by shape parameters is 83%, 67%, and 59%,

respectively. This trend indicates that under low to moderate wind speed conditions, the particle geometry has a more significant role in adjusting aerodynamic characteristics. However, under high wind speed conditions, wind effects dominate, and the influence of geometry on vertical velocity gradually decreases. Sand particles with higher shape parameters, due to their larger surface area and complex structure, can exchange momentum with the airflow more effectively, showing higher vertical acceleration capacity across all wind speed ranges. This indicates that wind speed and geometry work together on the vertical maximum velocity of sand particles, but the dominant factor shifts with the change in wind speed. At low to moderate wind speeds, shape parameters and axis ratios significantly affect the vertical momentum transfer by changing the symmetry, surface area, and wind-facing characteristics of the particles. However, under high wind speed conditions, wind effects become the decisive factor.

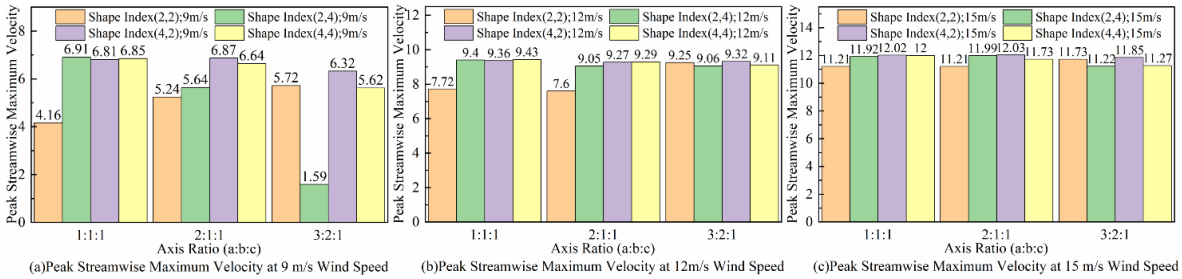

Fig. 13 - Vertical peak velocity under different wind speeds and sand particle shapes

CONCLUSIONS

This study uses a CFD–DEM method to reveal the hierarchical control of wind speed and grain geometry in aeolian sand transport.

(1) Wind speed is the primary factor controlling transport intensity. As wind speed increases, bed erosion becomes stronger, particle response becomes faster, and the transport process exhibits three stages of acceleration, stabilization, and decay. In this process, both mean and maximum velocities in the horizontal and vertical directions increase, and their peaks occur earlier, showing that airflow energy dominates transport intensity and the timing of saltation.

(2) For mean velocity in the streamwise direction, the effect of the axis ratio is stronger than that of shape parameters. Changes in axis ratio cause a maximum velocity variation of 96%, while shape parameters cause 53%. Further analysis shows that the effect of shape parameters is stronger for low-axis-ratio grains (53%) but weaker for high-axis-ratio grains (38%).

(3) Maximum velocity shows a coupled effect of axis ratio and wind speed. At wind speeds of 9, 12, and 15 m/s, the maximum variations under different axis ratios are: 39.8%, 18.1%, and 6.7% for 1:1:1; 17.9%, 16.0%, and 6.5% for 2:1:1; and 74.8%, 2.7%, and 5.3% for 3:2:1. The results show that higher wind speed reduces the influence of shape parameters on maximum velocity.

(4) In the vertical direction, the effect of shape parameters is stronger than that of the axis ratio. Changes in axis ratio cause variations in the mean velocity of less than 74.4%, while shape parameters cause variations of up to 91.6%. This indicates that shape parameters play a more important role in vertical momentum transfer.

(5) The vertical maximum velocity shows opposite trends with axis ratio: it decreases for shape parameters (2,4), (4,2), and (4,4), but increases for (2,2). Under the same axis ratio, the vertical maximum velocity increases with shape parameters, but this effect becomes weaker as wind speed increases. At 9, 12, and 15 m/s, the maximum variations caused by shape parameters are 83%, 67%, and 59%, respectively.

In summary, wind speed is the primary driver of aeolian sand transport, axis ratio is secondary in controlling streamwise velocity, and shape parameters exert stronger nonlinear effects on vertical momentum transfer and velocity, especially at low to moderate wind speeds. This study reveals the hierarchical control of wind speed and particle geometry and emphasizes the existence of nonlinear coupling effects. Future work should extend to turbulent flows, irregular particle geometries, and natural sand mixtures to improve understanding of sand transport mechanisms and enhance model predictions.

ACKNOWLEDGEMENTS

The work reported above was supported by the Natural Science Foundation of China (12362033), Xinjiang Uygur Autonomous Region 'Two Regions' Science and Technology Development Program of China (2023LQ01001).

REFERENCES

[1] AbdelRahman, M. A. E. (2023). An overview of land degradation, desertification and sustainable land management using GIS and remote sensing applications. *Rendiconti Lincei-Scienze Fisiche E Naturali*, *34*(3), 767-808. https://doi.org/10.1007/s12210-023-01155-3

[2] Akhtar-Schuster, M., Stringer, L. C., Metternicht, G., Barger, N. N., Chotte, J.-L., & Kust, G. (2022). Assessing the Impact of Science in the Implementation of the United Nations Convention to Combat Desertification. *Land*, *11*(4), Article 568. https://doi.org/10.3390/land11040568

[3] Anderson, R. S., & Haff, P. K. (1988). Simulation of eolian saltation. *Science (New York, N.Y.)*, *241*(4867), 820-823. https://doi.org/10.1126/science.241.4867.820

[4] Bagnold, R. A. (2012). The physics of blown sand and desert dunes. *Courier Corporation*.

[5] Cao, G., Pan, L., & Xu, K. (2022). High-order gas-kinetic scheme with parallel computation for direct numerical simulation of turbulent flows [Article]. *Journal of Computational Physics*, *448*, Article 110739. https://doi.org/10.1016/j.jcp.2021.110739

[6] Dammala, P. K., Kolli, S., Garaga, R., Reddy, K. R., & Kumar, P. (2025). Aeolian sand dune fixation - critical review of measures, challenges and future perspectives with a case study on Thar Desert. *Catena*, *250*, Article 108786. https://doi.org/10.1016/j.catena.2025.108786

[7] Huang, J., Yu, H., Guan, X., Wang, G., & Guo, R. (2016). Accelerated dryland expansion under climate change. *Nature Climate Change*, *6*(2), 166-+. https://doi.org/10.1038/nclimate2837; 10.1038/NCLIMATE2837

[8] Kruggel-Emden, H., Rickelt, S., Wirtz, S., & Scherer, V. (2008). A study on the validity of the multi-sphere Discrete Element Method. *Powder Technology*, *188*(2), 153-165. https://doi.org/10.1016/j.powtec.2008.04.037

[9] Launder, B. E., & Spalding, D. B. (1983). The numerical computation of turbulent flows. *In Numerical prediction of flow, heat transfer, turbulence and combustion* (pp. 96-116). Elsevier. https://doi.org/10.1016/0045-7825(74)90029-2

[10] Liu, X., Yi, Z., Li, J., Lu, L., Cui, L., & Tao, Q. (2025). Influence of sand size on motion and transport characteristics of wind-sand two-phase flow in desert environments. *Particuology*, *103*, 104-116. https://doi.org/10.1016/j.partic.2025.05.019

[11] Liu, Z., Ma, H., & Zhao, Y. (2021). CFD-DEM Simulation of Fluidization of Polyhedral Particles in a Fluidized Bed. *Energies*, *14*(16), Article 4939. https://doi.org/10.3390/en14164939

[12] Liu, Z., & Zhao, Y. (2020). Multi-super-ellipsoid model for non-spherical particles in DEM simulation. *Powder Technology*, *361*, 190-202. https://doi.org/10.1016/j.powtec.2019.09.042

[13] Lu, G., Third, J. R., & Mueller, C. R. (2015). Discrete element models for non-spherical particle systems: From theoretical developments to applications. *Chemical Engineering Science*, *127*, 425-465. https://doi.org/10.1016/j.ces.2014.11.050

[14] Lv, L., & Zhao, B. (2025). From shape to behavior: A synthesis of non-spherical particle dynamics in air. *Particuology*, *96*, 218-243, Article 1674-2001(2025)96<218:Fstbas>2.0.Tx;2-8. https://doi.org/10.1016/j.partic.2024.11.005

[15] Marshall, J., Fenton, L. K., & Harlow, J. J. B. (2021). Limitations of applying grain weight similitude in aeolian studies with NASA Mars Wind Tunnel. *Aeolian Research*, *53*, Article 100732. https://doi.org/10.1016/j.aeolia.2021.100732

[16] Podlozhnyuk, A., Pirker, S., & Kloss, C. (2017). Efficient implementation of superquadric particles in Discrete Element Method within an open-source framework. *Computational Particle Mechanics*, *4*(1), 101-118. https://doi.org/10.1007/s40571-016-0131-6

[17] Qiao, T., Liu, L., & Ji, S. (2022). Superquadric DEM-SPH coupling method for interaction between non-spherical granular materials and fluids. *Particuology*, *71*, 20-33. https://doi.org/10.1016/j.partic.2022.01.012

[18] Shao, Y. P., & Lu, H. (2000). A simple expression for wind erosion threshold friction velocity. *Journal of Geophysical Research-Atmospheres*, *105*(D17), 22437-22443. https://doi.org/10.1029/2000jd900304

[19] Song, X.-P., Hansen, M. C., Stehman, S. V., Potapov, P. V., Tyukavina, A., Vermote, E. F., & Townshend, J. R. (2018). Global land change from 1982 to 2016 [Article]. *Nature*, *560*(7720), 639-+. https://doi.org/10.1038/s41586-018-0411-9

[20] Spinoni, J., Barbosa, P., Cherlet, M., Forzieri, G., McCormick, N., Naumann, G.,…Dosio, A. (2021). How will the progressive global increase of arid areas affect population and land-use in the 21st century? *Global and Planetary Change*, *205*, Article 103597. https://doi.org/10.1016/j.gloplacha.2021.103597

[21] Tang, X., Wang, S., Jin, X., & Shen, Y. (2024). Super-quadric CFD-DEM modelling of chip-like particle-liquid flow in a rotary drum. *Powder Technology*, *435*, Article 119363. https://doi.org/10.1016/j.powtec.2024.119363

[22] Wang, Z., Ren, S., & Huang, N. (2014). Saltation of Non-Spherical Sand Particles. *Plos One*, *9*(8), Article e105208. https://doi.org/10.1371/journal.pone.0105208

[23] Yang, J., Zhang, Y., Liu, D., & We, X. (2010). CFD-DEM simulation of three-dimensional aeolian sand movement. *Science China-Physics Mechanics & Astronomy*, *53*(7), 1306-1318. https://doi.org/10.1007/s11433-010-4038-6

[24] Zhang, P., Sherman, D. J., & Li, B. (2021). Aeolian creep transport: A review. *Aeolian Research*, *51*, Article 100711. https://doi.org/10.1016/j.aeolia.2021.100711

[25] Zhang, Q., Deal, E., Perron, J. T., Venditti, J. G., Benavides, S. J., Rushlow, M., & Kamrin, K. (2025). Discrete Simulations of Fluid-Driven Transport of Naturally Shaped Sediment Particles. *Journal of Geophysical Research-Earth Surface*, *130*(5), Article e2024JF007937. https://doi.org/10.1029/2024jf007937

[26] Zheng, J. X., & Hryciw, R. D. (2016). Roundness and Sphericity of Soil Particles in Assemblies by Computational Geometry. *Journal of Computing in Civil Engineering*, *30*(6), Article 04016021. https://doi.org/10.1061/(asce)cp.1943-5487.0000578

[27] Zhu, H. P., Zhou, Z. Y., Yang, R. Y., & Yu, A. B. (2007). Discrete particle simulation of particulate systems: Theoretical developments. *Chemical Engineering Science*, *62*(13), 3378-3396. https://doi.org/10.1016/j.ces.2006.12.089

[28] Zong, Q., & Wu, X. (2024). A review of computational fluid dynamics (CFD) methodology and analysis on airflow and sand transport over aeolian landforms. *Catena*, *241*, Article 108010. https://doi.org/10.1016/j.catena.2024.108010